Effects of Concave Curvature on Boundary Layer Transition Under High Freestream Turbulence Conditions

Michael P. Schultz
e-mail: mschultz@usna.edu

Ralph J. Volino
e-mail: volino@usna.edu

Department of Mechanical Engineering,
United States Naval Academy,
Annapolis, MD 21402

An experimental investigation has been carried out on a transitional boundary layer subject to high (initially 9%) freestream turbulence, strong acceleration ($K=(\nu/U_w^2)\times(dU_w/dx)$ *as high as* 9×10^{-6}), *and strong concave curvature (boundary layer thickness between 2% and 5% of the wall radius of curvature). Mean and fluctuating velocity as well as turbulent shear stress are documented and compared to results from equivalent cases on a flat wall and a wall with milder concave curvature. The data show that curvature does have a significant effect, moving the transition location upstream, increasing turbulent transport, and causing skin friction to rise by as much as 40%. Conditional sampling results are presented which show that the curvature effect is present in both the turbulent and nonturbulent zones of the transitional flow.* [DOI: 10.1115/1.1522410]

Introduction

Boundary layer transition is influenced by a number of factors, including streamwise pressure gradient, freestream turbulence intensity (FSTI), surface curvature, compressibility, and surface roughness. In gas turbine environments, Mayle [1] states that a substantial fraction of the boundary layer on both sides of a gas turbine airfoil may be transitional. The extended transition zones exist due to strong favorable pressure gradients, found on both the pressure side and the leading section of the suction side, which stabilize the boundary layer and delay transition in spite of the high freestream disturbance levels in gas turbine environments. The ability to model and predict high FSTI transition is important since heat transfer rates, skin friction coefficients, and in some cases boundary layer separation depend strongly on the state of the boundary layer with respect to transition. Improved transition models and turbine designs depend, therefore, on a better understanding of high FSTI transition.

The role of surface curvature on high FSTI transition is not fully understood. Mayle [1] states that transition onset is controlled by the freestream turbulence and the periodic unsteadiness caused by wakes from upstream airfoils. He notes that the turbulent spot production rate, which determines the length of the transition region, is controlled primarily by the freestream disturbance and the streamwise pressure gradient, but that curvature may play a secondary role. The extent of this secondary role is largely unknown, as only limited data exist from convex surfaces and ''virtually no reliable data'' are available from concave surfaces for computation of spot production rates, [1]. Determining the significance of curvature is potentially important for improved turbine design. If curvature is not significant, both modeling of transitional boundary layers and future experimental studies may be simplified, as results from flat-plate studies may be directly applied to curved airfoils. If curvature is found to be significant, its effects should be incorporated into future transition models.

Reasonable arguments can be made both for and against the importance of curvature on high FSTI transition. Low FSTI results suggest that curvature is important. Görtler [2] determined theoretically that convex curvature is stabilizing and that concave curvature is destabilizing. He predicted the formation of streamwise vortices (now known as Görtler vortices) on concave surfaces. Liepmann [3] confirmed these results experimentally under low FSTI conditions. He showed that convex curvature only slightly delays transition, but that concave curvature can cause transition to occur significantly earlier. Transition occurred when the Görtler number, G, was between 6 and 9, decreasing with the FSTI. These results have been confirmed in several subsequent studies. Floryan [4] and Saric [5] provide reviews. Volino and Simon [6] provide recent documentation from a zero pressure gradient case, and Finnis and Brown [7] considered a favorable pressure gradient case. In a low FSTI, fully turbulent boundary layer, Simonich and Moffat [8] showed that concave curvature of strength comparable to gas turbine conditions resulted in about a 20% enhancement in heat transfer over flat-plate results.

While the low FSTI studies show the importance of concave curvature, the results of high FSTI investigations are less clear. Data from fully turbulent boundary layers again suggest that curvature is important. Kim et al. [9] documented cases with inlet FSTI of 8% on both flat and concave walls, and showed increased turbulent activity and an enhancement of heat transfer by about 16% on the concave wall. Kestoras and Simon [10] documented a boundary layer with 8% inlet FSTI moving from a concave wall onto a flat wall. They showed an almost immediate drop in turbulence within the boundary layer as the flow moved onto the flat wall. They postulated a synergistic effect between curvature and freestream turbulence, stating that when concave curvature and high FSTI are combined, the freestream eddies are able to penetrate closer to the wall than in a flat wall flow, resulting in significantly higher transport within the boundary layer.

Only a few studies have documented transition with high FSTI. On surfaces subject to zero streamwise pressure gradients, Blair [11], Sohn and Reshotko [12], and Kim et al. [9] all showed that at FSTI above about 3%, transition occurred rapidly near the leading edge of a test surface. Hence, little documentation of transition is provided in these cases. Kim et al. [9] included a concave curvature case, and found no evidence of Görtler vortices. They proposed that the enhanced turbulent transport caused by the high FSTI and early transition lowered the effective Görtler number and suppressed the formation of the vortices. Since Görtler vortices change the transition mechanism and promote early transition under low FSTI conditions, [6], their absence under high FSTI might suggest that curvature does not play a strong role in high

Contributed by the Fluids Engineering Division for publication in the JOURNAL OF FLUIDS ENGINEERING. Manuscript received by the Fluids Engineering Division July 12, 2001; revised manuscript received July 26, 2002. Associate Editor: K. B. M. Q. Zaman.

 Copyright © 2003 by ASME

Downloaded 23 Jul 2008 to 131.122.82.145. Redistribution subject to ASME license or copyright; see http://www.asme.org/terms/Terms_Use.cfm

FSTI transition. Riley et al. [13] considered zero pressure gradient cases on concave walls with inlet FSTI as high as 7.2%. Their results indicate that with very strong curvature ($(r/\theta_s)^{0.5}<20$), transition start is delayed relative to flat wall results. They reported the presence of Görtler vortices, and attributed the delayed transition to increased near-wall velocity gradients caused by the vortices. In cases with curvature representative of gas turbine conditions ($(r/\theta_s)^{0.5}>30$), as indicated by Mayle [1]), Riley et al. [13] showed no significant difference in transition start between concave and flat wall results. They did not provide a correlation for transition end.

Extended transition regions do occur when high FSTI is combined with strong acceleration. Results are available from turbine cascade and rotating rig studies (e.g., Halstead et al. [14]), but in these cases the effects of airfoil curvature, while present, cannot be isolated. Volino and Simon [15–17] considered transition along a concave wall with inlet FSTI of 8% and acceleration with K as high as 9×10^{-6}. Acceleration rates, Reynolds numbers and FSTI were typical of the pressure side of a gas turbine airfoil. The strength of curvature, $(r/\theta_s)^{0.5}=53$, was mild relative to gas turbine conditions. An extended transition region, with intermittent turbulent and nonturbulent zones, covered most of the test surface. Although detailed documentation of the transition was provided, no comparison case from a flat wall was available, so the effect of the concave curvature could not be determined. Volino and Simon [17] stated that the curvature effect was probably small, since the strong acceleration, by suppressing the growth of the boundary layer, kept the strength of curvature low. In contrast, Volino [18] presented a model incorporating freestream turbulence and curvature effects and used it to predict that the curvature effect in the Volino and Simon [15–17] case might be substantial. As stated above, no experimental data were available to verify the prediction.

The present study addresses the significance of concave curvature directly. The case presented by Volino and Simon [15–17] has been reproduced on a flat test wall, and a concave wall with strong curvature ($(r/\theta_s)^{0.5}=27$). The flat wall results were presented in detail by Volino et al. [19]. In the present paper the concave wall results are presented and compared to the flat wall results and the weaker concave curvature case of Volino and Simon [15–17].

Experiments

Facility and Measurements. All experiments were conducted in the same low speed wind tunnel described in detail by Volino et al. [19] and shown in Fig. 1. The only change to the facility for the present study was the replacement of a flat-plate test section with a curved, converging channel. The facility is very similar to that used by Volino and Simon [17], again with the exception of the curvature of the test wall. One side of the present test section is a concave curved Plexiglas surface of 0.69 m width and 0.80 m length, which serves as the test wall. This wall has a constant radius of curvature of 25.4 cm. Pressure taps are installed along its spanwise centerline. At the leading edge of the test wall a slot is used to bleed off the boundary layer which grows in the development section between the turbulence generator and the leading edge. Opposite the test wall is a flexible convex wall that can be adjusted to set the desired pressure gradient along the test wall. For the present study the inlet velocity is set to 4.6 m/s and the velocity gradient along the wall is held constant at 13.9 s^{-1}, matching the previous flat wall, [19], and mild concave curvature, [17], cases.[1] The acceleration parameter, K, drops from a maximum of 9×10^{-6} at the inlet to the test section to 1×10^{-6} at the last measurement station. The FSTI at the inlet to the test section is 8.6%, based on all three components of the fluctuating velocity. Further details of the freestream turbulence including spectra and length scales are given in Volino et al. [19]. Within the test section, the streamwise component of the freestream turbulence, $\overline{u'_\infty}$, remains nearly constant at ~0.35 m/s, but $\overline{v'_\infty}$ increases from 0.50 m/s to 0.73 m/s. On the flat wall, $\overline{u'_\infty}$ decreased in the streamwise direction while $\overline{v'_\infty}$ remained nearly constant. It should be noted, however, that these values are based on data at the measurement point most distant from the wall ($y=30$ mm). While $\overline{u'_\infty}$ and $\overline{v'_\infty}$ on the flat wall and $\overline{u'_\infty}$ on the concave wall reach their freestream value by this location, $\overline{v'_\infty}$ is still changing with distance from the wall at several streamwise stations on the concave wall. Freestream turbulence intensity (normalized using the local freestream velocity) drops in the streamwise direction in both the concave and flat wall cases, mainly due to the increasing freestream velocity. Values of K through the test section, measurement locations, and other parameters are shown in Table 1.

Velocity profile measurements were made at nine streamwise stations along the centerline of the test wall using a single sensor, boundary layer type hot-wire probe (TSI model 1218-T1.5), a boundary layer cross-wire probe (TSI model 1243-T1.5) and a constant-temperature hot-wire anemometer (TSI model IFA-100). The probes were moved normal to the wall at each station using a manual traversing stage with a minimum increment of 10 μm. At each position in the velocity profiles, data were acquired for 26 seconds at a 20 kHz sampling rate (2^{19} data points). The hot-wire signals were low-pass filtered at 10 kHz. All raw data were stored. Sampling at 20 kHz provided essentially continuous velocity traces for subsequent processing as detailed in Volino et al. [19]. Mean and rms fluctuating velocities in the streamwise and wall-normal directions were computed from the instantaneous data. Uncertainties in these quantities are 3–5% except in the very near wall region ($y^+<5$) where near-wall corrections (Wills [22]) are applied to the mean velocity. Uncertainty in the turbulent shear stress, $-\overline{u'v'}$, is 10%. Skin friction coefficients were determined using a technique whereby τ_w was adjusted until the U^+ versus y^+ data fit profiles computed using near-wall similarity, as described by Volino and Simon [23]. This technique accounts for pressure gradient effects on the near wall profile. Uncertainty in C_f is 8%. Boundary layer thicknesses were determined from the mean velocity profiles. Uncertainties in the momentum and displacement thicknesses are 10%. These uncertainties include bias errors which tend to cancel such that the uncertainty in the shape factor, H, is 7%. The intermittency function, which indicates whether the boundary layer is instantaneously turbulent or nonturbulent, was calculated using both the instantaneous streamwise velocity, u, and the instantaneous turbulent shear stress, $-u'v'$, as described by Volino et al. [19]. The overall uncertainty in the time-averaged intermittency, γ, is 0.1. The instantaneous intermittency function was used to separate the turbulent and nonturbulent

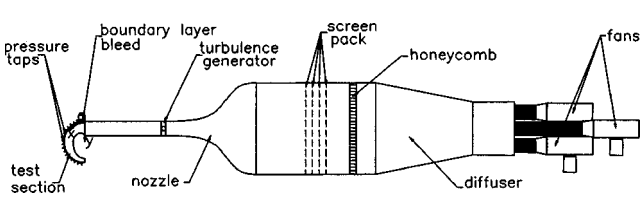

Fig. 1 Schematic of the test facility

[1]The nominal "freestream" velocity for the concave wall cases is not so clear as in the corresponding flat wall case. On a flat wall, the velocity gradient $\partial U/\partial y$ approaches zero outside the boundary layer, so the freestream velocity is independent of the distance from the wall. Curvature induces a nonzero $\partial U/\partial y$, which under low FSTI conditions approaches the potential flow solution for a curved channel. With high FSTI, however, the combination of streamwise curvature and freestream turbulence results in cross transport of momentum, as described by Eckert [20], and deviation from the potential flow solution. The gradient $\partial U/\partial y$ is approximately constant in the freestream, so following the procedure of Kestoras and Simon [21], a straight line is fit to the mean velocity data in the freestream at each station and extrapolated to the wall ($y=0$). This extrapolated velocity, designated U_w, is used as the freestream velocity for the concave wall case.

Downloaded 23 Jul 2008 to 131.122.82.145. Redistribution subject to ASME license or copyright; see http://www.asme.org/terms/Terms_Use.cfm

Table 1 Flow parameters at measurement stations

St	x [m]	U_w [m/s]	$\frac{\overline{u'_\infty}}{U_w}$ [%]	$\frac{\overline{v'_\infty}}{U_w}$ [%]	K $\times 10^6$	γ_{pk} [%]	$\delta_{99.5}$ [mm]	Re_x $\times 10^{-5}$
1	0.119	5.94	6.0	8.1	6.01	12.	4.89	0.39
2	0.189	7.25	4.5	7.3	4.06	11.	4.69	0.91
3	0.268	8.49	3.6	6.6	2.96	24.	5.37	1.51
4	0.345	9.53	3.2	6.0	2.35	49.	6.09	2.19
5	0.433	11.0	2.8	5.6	1.79	68.	7.00	3.14
6	0.503	12.0	2.6	5.2	1.50	81.	9.29	3.98
7	0.581	13.0	2.5	5.0	1.27	91.	10.8	5.00
8	0.659	14.0	2.4	4.9	1.10	97.	13.9	6.11
9	0.736	14.6	2.4	4.8	1.00	99.	12.6	7.13

St	Re_θ	H	G	$C_f \times 10^3$	Re_θ	H	$C_f \times 10^3$	Re_θ	H	$C_f \times 10^3$
	composite				non-turbulent			turbulent		
1	133	1.79	5.3	9.0	134	1.77	9.0	124	1.54	14.3
2	143	1.80	4.9	8.0	140	1.81	8.0	162	1.45	13.0
3	172	1.75	6.0	7.2	156	1.83	7.2	241	1.41	10.8
4	193	1.71	6.7	7.3	147	1.88	7.0	321	1.38	9.7
5	247	1.59	9.0	7.0	152	1.91	6.7	378	1.38	8.4
6	310	1.53	12.2	7.0	155	1.93	6.5	509	1.33	8.0
7	384	1.44	16.1	7.1	159	1.91	6.4	598	1.30	7.7
8	461	1.44	20.4	7.0	160	1.96	6.0	777	1.27	7.2
9	483	1.45	21.4	6.8	152	2.04	5.7	788	1.29	7.0

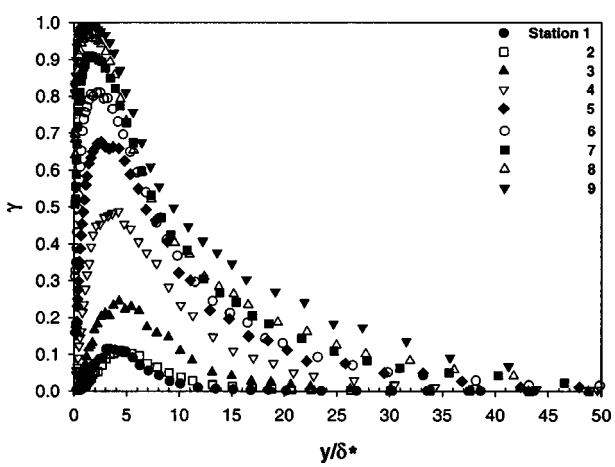

Fig. 2 Intermittency profiles based on u

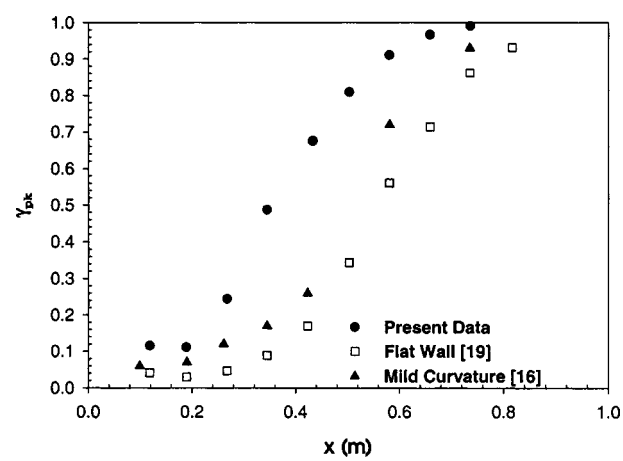

Fig. 3 Intermittency factor versus streamwise distance

zones of the boundary layer for conditional sampling. In the figures which follow, data points are shown for the nonturbulent zone only when the local $\gamma < 95\%$, and for the turbulent zone only when $\gamma > 5\%$. Bulk parameters such as C_f are presented when $\gamma_{pk} < 95\%$ and $\gamma_{pk} > 5\%$ for the nonturbulent and turbulent zones, respectively.

Results

Intermittency. Intermittency profiles for the nine measurement stations are shown in Fig. 2. These results were computed using the instantaneous streamwise velocity, u. Although not presented here, intermittency profiles based on the instantaneous tur-

Table 2 Transition start and end locations

Case	$(r/\theta_s)^{0.5}$	x_s [m]	x_e [m]	$\hat{n}\sigma \times 10^{11}$
Flat [19]	∞	0.29	0.98	4.2
Mild Curve [17]	53	0.23	0.90	5.5
Strong Curve	27	0.12	0.75	10.

Downloaded 23 Jul 2008 to 131.122.82.145. Redistribution subject to ASME license or copyright; see http://www.asme.org/terms/Terms_Use.cfm

bulent shear stress always agreed with those in Fig. 2 to within 0.10 and were generally within 0.05. The intermittency remains nonzero well away from the wall, to y/δ^* as high as 40. In the flat wall case, Volino et al. [19] showed γ approaching zero by $y/\delta^*=10$. Something in the concave wall case promotes turbulence well away from the wall. The peak intermittency in each profile is shown in Fig. 3 and compared to results from the flat wall and mild curvature cases. The intermittency remains fairly low ($\gamma_{pk}\sim 10\%$) for the first two stations of the strong curvature case and then starts to rise. Note that even at the first station, the intermittency is higher than that measured in the other two cases. For all these cases, the beginning of the rise in γ corresponds to K dropping below 3×10^{-6}. In low FSTI boundary layers, $K>3\times 10^{-6}$ leads to relaminarization (Jones and Launder [24]). By the last station, transition is complete in the strong curvature case, whereas the flat and mildly curved wall cases are only approaching the end of transition. Following the technique of Narasimha [25], as modified by Volino and Simon [26], the function

$$f(\gamma_{pk})=(-\ln(1-\gamma_{pk}))^{1/2} \tag{1}$$

can be computed based on the peak intermittency at each station and plotted versus streamwise location. The data in these coordinates tend to lie along a straight line. The line may be extrapolated to $f(\gamma_{pk}=0)=0$ and $f(\gamma_{pk}=0.99)=2.146$, corresponding to the beginning and end of transition. Transition start and end locations for the three cases are listed in Table 2. Figure 4 shows γ_{pk} plotted versus dimensionless streamwise location within transition. Also shown is the theoretical curve

$$\gamma_{pk}=\exp\left(-4.6\left(\frac{x-x_s}{x_e-x_s}\right)^2\right) \tag{2}$$

based on the Dhawan and Narasimha [27] transition model. Agreement between the data and theory is good. Differences from Eq. (2) are seen at low γ in all the cases. This is termed "subtransition" [25] and is expected in favorable pressure gradient flows. The Dhawan and Narasimha [27] model assumes a concentrated breakdown or formation of turbulent spots at the transition start location. In fact, spots are formed over some finite distance in the streamwise direction in a distributed breakdown. Favorable pressure gradients stabilize the boundary layer and extend this region, resulting in the subtransition. The presence of the subtransition means that the actual start of transition does not occur at the x_s location given in Table 2. The x_s and x_e value do, however, indicate the rate at which transition proceeds. The mild curvature case completes transition slightly upstream of the flat wall case, and the strong curvature case completes transition well upstream of the other two cases. Since curvature is the only difference between the cases, it is clear that concave curvature has a significant effect on transition.

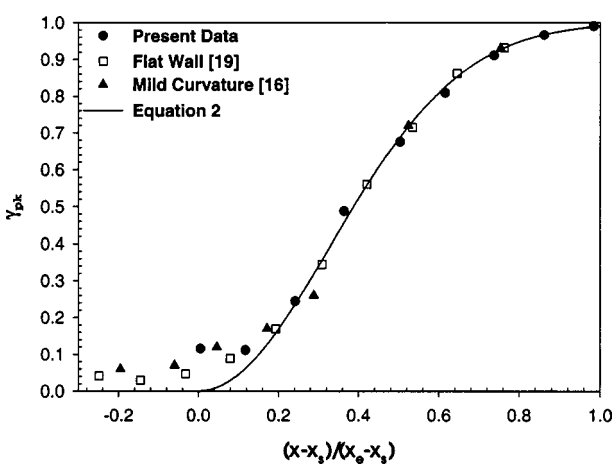

Fig. 4 Peak intermittency in profile versus dimensionless streamwise location

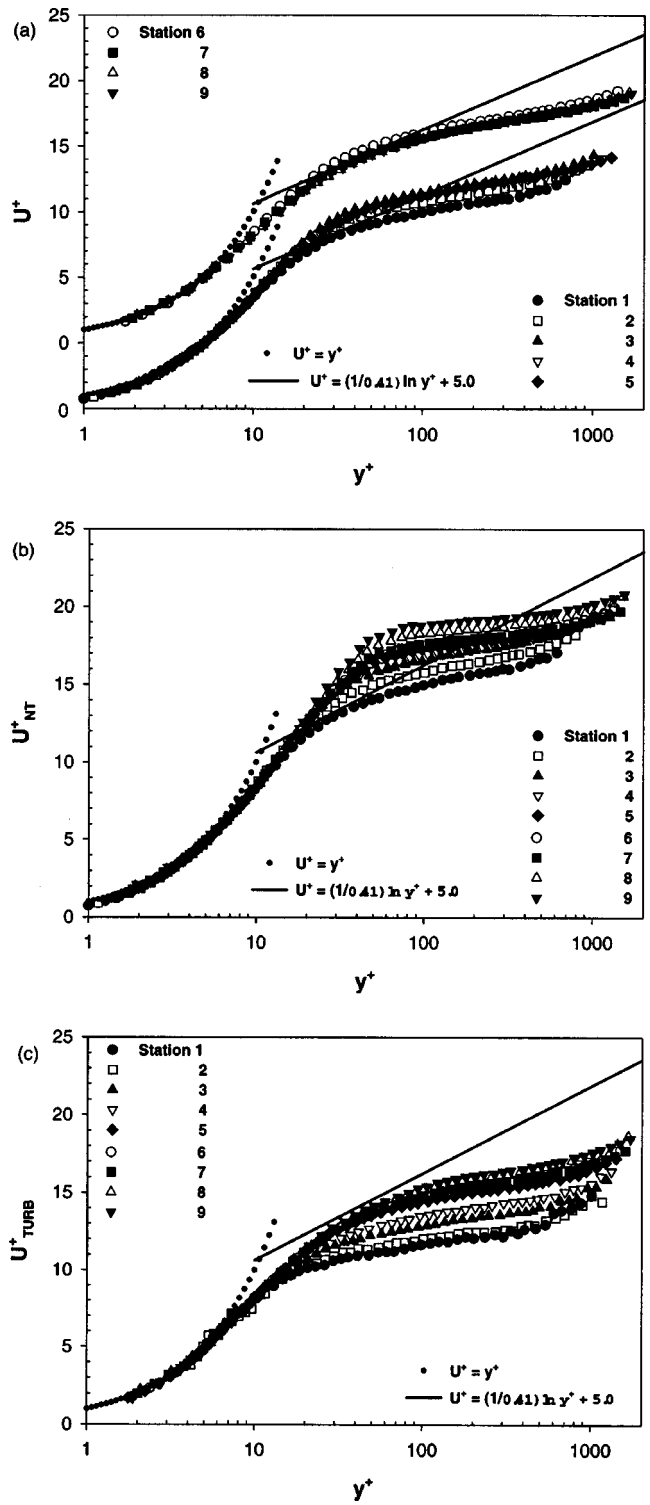

Fig. 5 Mean velocity profiles in wall coordinates: (*a*) composite; (*b*) nonturbulent; (*c*) turbulent

The dimensionless turbulent spot propagation rate (Mayle [1]) may be computed as

$$\hat{n}\sigma=\frac{4.6\nu^2\overline{U}_\infty}{(x_e-x_s)^2U_s^3} \tag{3}$$

Downloaded 23 Jul 2008 to 131.122.82.145. Redistribution subject to ASME license or copyright; see http://www.asme.org/terms/Terms_Use.cfm

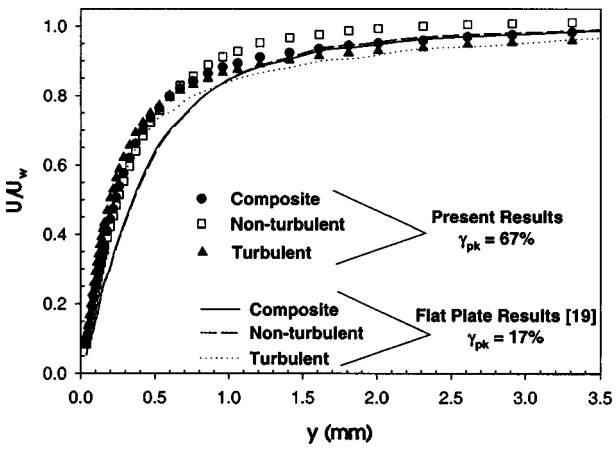

Fig. 6 Mean velocity profile for Station 5

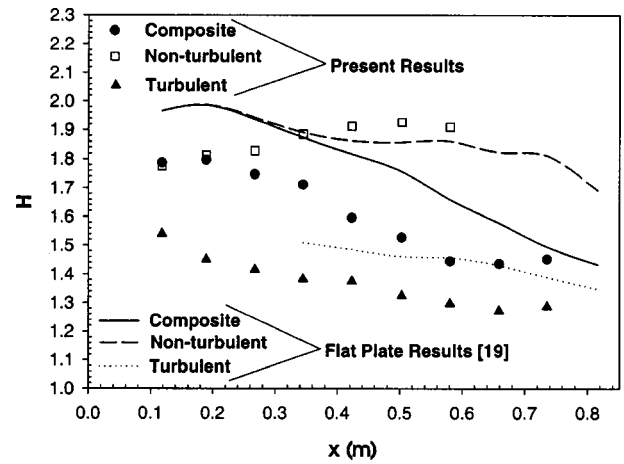

Fig. 8 Shape factor versus streamwise distance

where $\overline{U}_\infty$ is the average freestream velocity in the transition region. In the strong curvature case $\hat{n}\sigma = 1.0\times10^{-10}$. For the flat wall case and the mild curvature case, $\hat{n}\sigma$ was 4.2×10^{-11} and 5.5×10^{-11}, respectively. These values are in agreement with the trends reported by Mayle [1] for other favorable pressure gradient cases and are three to five times less than would be expected for a zero pressure gradient case with the same FSTI at the beginning of transition. It appears that wall curvature, FSTI and pressure gradient are all important parameters in determining the spot propagation rate.

Mean Velocity Profiles. Mean velocity profiles for the nine measurement stations of the strong curvature case are presented in Fig. 5 in wall coordinates. Figure 5(a) shows the composite (unconditioned) profiles. Figures 5(b) and 5(c) show turbulent and nonturbulent zone results from conditional sampling of the data. The composite profiles vary only slightly through Station 5. For the remaining downstream stations, the profiles collapse to a turbulent-like shape. Even the most upstream stations do not exhibit the laminar-like shape that was seen in the flat wall results of Volino et al. [19]. At Stations 7–9, where the acceleration rate has dropped to $K<1.5\times10^{-6}$ and transition is complete or nearly so, the profiles agree with the zero pressure gradient law of the wall, although the log-law region is quite small. The short log-law region is a consequence of the combined concave curvature and high FSTI that gives rise to significant momentum transport and result in a large, negative wake strength. The nonturbulent zone profiles (Fig. 5(b)) exhibit a laminar-like shape, even at the end of transition, as was also seen in the flat wall case. The turbulent zone profiles (Fig. 5(c)) exhibit a more turbulent-like shape, and the last five stations collapse. Note that the data at even the most downstream station falls slightly below the zero pressure gradient law of the wall, again due to the enhanced momentum transport in the outer part of the boundary layer. Examination of the results in [19] shows that this effect is not as strong on the flat wall, where there is better agreement with the zero-pressure gradient law of the wall.

Figure 6 shows the differences between the composite, nonturbulent, and turbulent profiles at Station 5, in the center of the transition zone ($\gamma_{pk}=0.67$). Also shown for comparison are the results for the flat wall at the same streamwise position, which was closer to the start of transition ($\gamma_{pk}=0.17$). On the concave wall, velocities in the near wall region are slightly higher in the turbulent zone than in the nonturbulent zone due to higher levels of turbulent mixing. Differences between the zones are not as dramatic as on the flat wall, however. While this might be attributed to the difference in the intermittency for the two cases at this streamwise position, it is also observed when comparing profiles from the two cases with the same intermittency and different streamwise locations. The enhanced mixing induced by the curvature results in higher near wall velocities, particularly in the nonturbulent zone. In the concave wall case, as in the flat wall case, the nonturbulent zone of the boundary layer never behaves as if it were laminar due to the freestream buffeting the boundary layer. This is explained further in Volino [18].

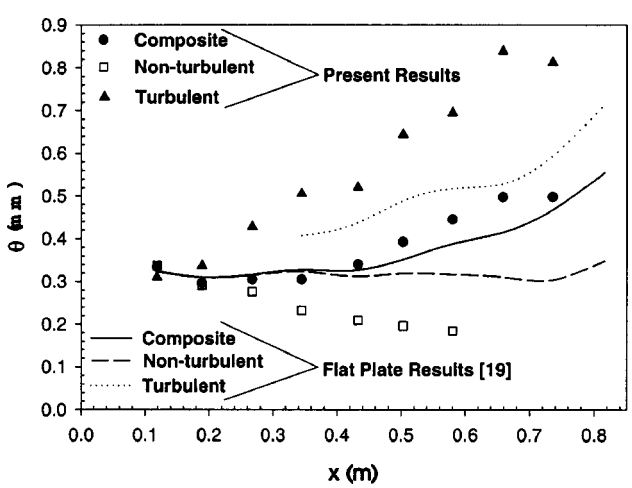

Fig. 7 Momentum thickness versus streamwise distance

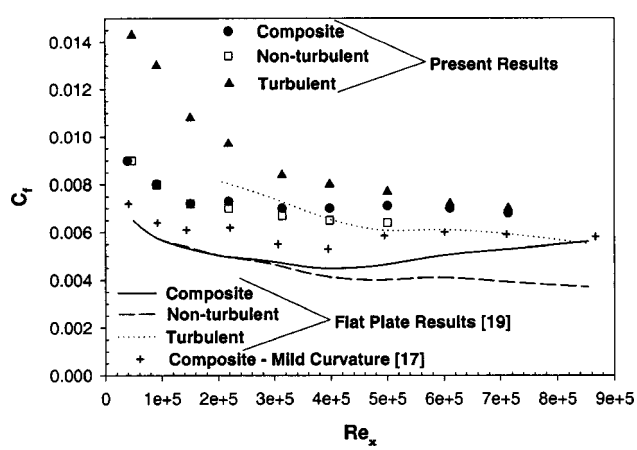

Fig. 9 Comparison of skin-friction coefficient

Downloaded 23 Jul 2008 to 131.122.82.145. Redistribution subject to ASME license or copyright; see http://www.asme.org/terms/Terms_Use.cfm

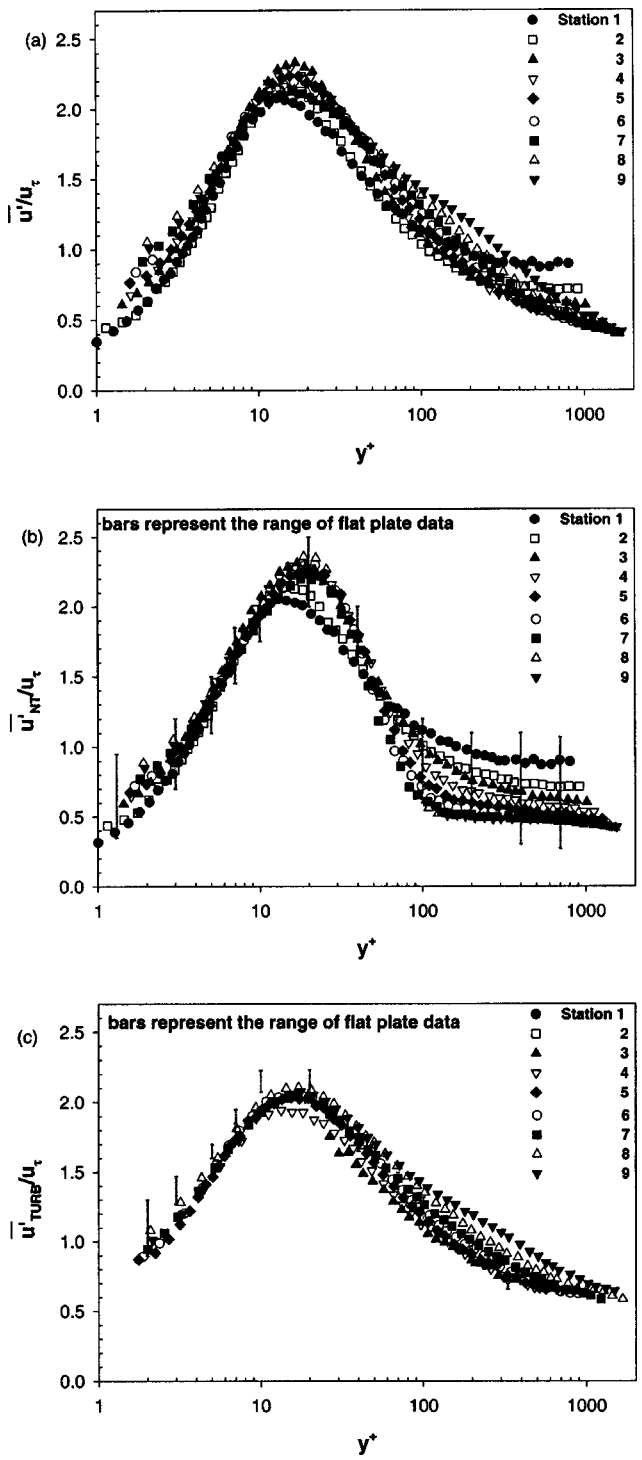

Fig. 10 Fluctuating streamwise velocity profiles in wall coordinates: (*a*) composite; (*b*) nonturbulent; (*c*) turbulent

Boundary Layer Growth. Figure 7 shows the momentum thickness plotted versus streamwise position. On the concave wall, the composite flow momentum thickness remains nearly constant through the first five stations and then increases as K drops and transition nears completion. In the nonturbulent zone, the momentum thickness drops somewhat in the streamwise direction. In contrast, the turbulent zone momentum thickness increases continuously. This is likely due to turbulent entrainment at the boundary layer edge, which appears to be more significant on the concave wall than the flat wall.

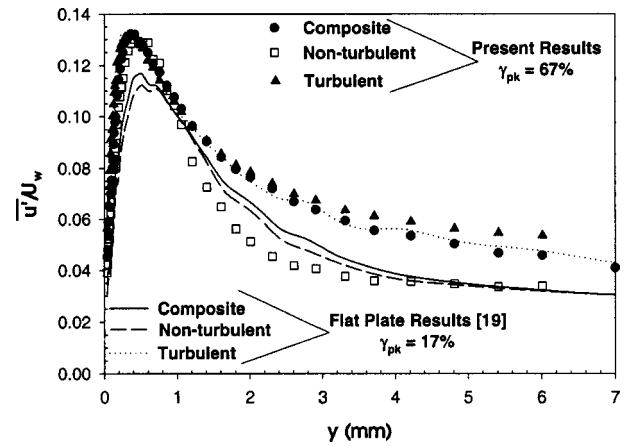

Fig. 11 Fluctuating streamwise velocity profile for Station 5

The shape factor, H, shown in Fig. 8, is an indicator of the state of the boundary layer with respect to transition. The composite flow shape factor drops from about 1.8 at Station 1 to 1.45 at Station 9. The decrease in H tracks the increase in γ_{pk} (Fig. 3). In the nonturbulent zone H increases slightly from 1.8 to about 2.0. A low FSTI laminar boundary layer on a flat wall with the same pressure gradient would have a shape factor of about 2.4. The shape factors below the laminar value agree with Fig. 6, which shows that the high FSTI makes the nonturbulent zone velocity profiles appear less laminar-like and more like those in the turbulent zone. In the turbulent zone, H drops from about 1.5 to 1.3. These values are significantly less than those for the flat wall case and suggest that the wall curvature promotes greater momentum transport in the turbulent zone even in a high FSTI, strongly accelerated boundary layer.

Skin Friction Coefficients. Skin friction coefficients, C_f, were computed from the mean velocity profiles and are plotted versus Re_x in Fig. 9. Composite flow results are presented for the flat wall, mild and strong curvature cases, and conditional sampling results are presented for the flat wall and strong curvature cases. The striking characteristic of the figure is that the nonturbulent, turbulent, and composite skin friction values in the strong curvature case are all significantly higher than in the flat wall case. The composite skin friction coefficient is as much as 56% higher and is an average of 42% higher than the flat wall case. The average increases in C_f in the nonturbulent and turbulent zone are 45% and 23%, respectively. These results indicate that wall curvature, even in the presence of strong acceleration and high FSTI, can lead to a significant increase in momentum transport in the boundary layer. The C_f values from the mild curvature case fall between the flat wall and strong curvature results as expected. The differences between the flat and curved wall cases shown in Figs. 5–9 are apparent even at the most upstream stations. This is not unreasonable since $G \approx 5$, and $(r/\theta_s)^{0.5} = 25$ by Station 1 of the strong curvature case.

Fluctuating Velocity. Figure 10 shows $\overline{u'}$ profiles in wall coordinates. The strong curvature composite flow results, shown in Fig. 10(a), are typical of transitional and turbulent boundary layers. The peak in $\overline{u'}/u_\tau$ occurs at $y^+ = 15$, and the magnitude of the peak is between 2 and 2.3. The nonturbulent and turbulent zone data are shown in Figs. 10(b) and 10(c), respectively. Included in these figures are bars showing the range of flat wall data from Volino et al. [19]. In the nonturbulent zone, the concave wall data show good agreement with the flat wall results. In the turbulent zone the data from all stations collapse, particularly near the wall, showing self-similarity throughout the transition region. In the near wall region $\overline{u'}/u_\tau$ on the concave wall is slightly but consistently reduced compared to the flat wall case. This indicates

Downloaded 23 Jul 2008 to 131.122.82.145. Redistribution subject to ASME license or copyright; see http://www.asme.org/terms/Terms_Use.cfm

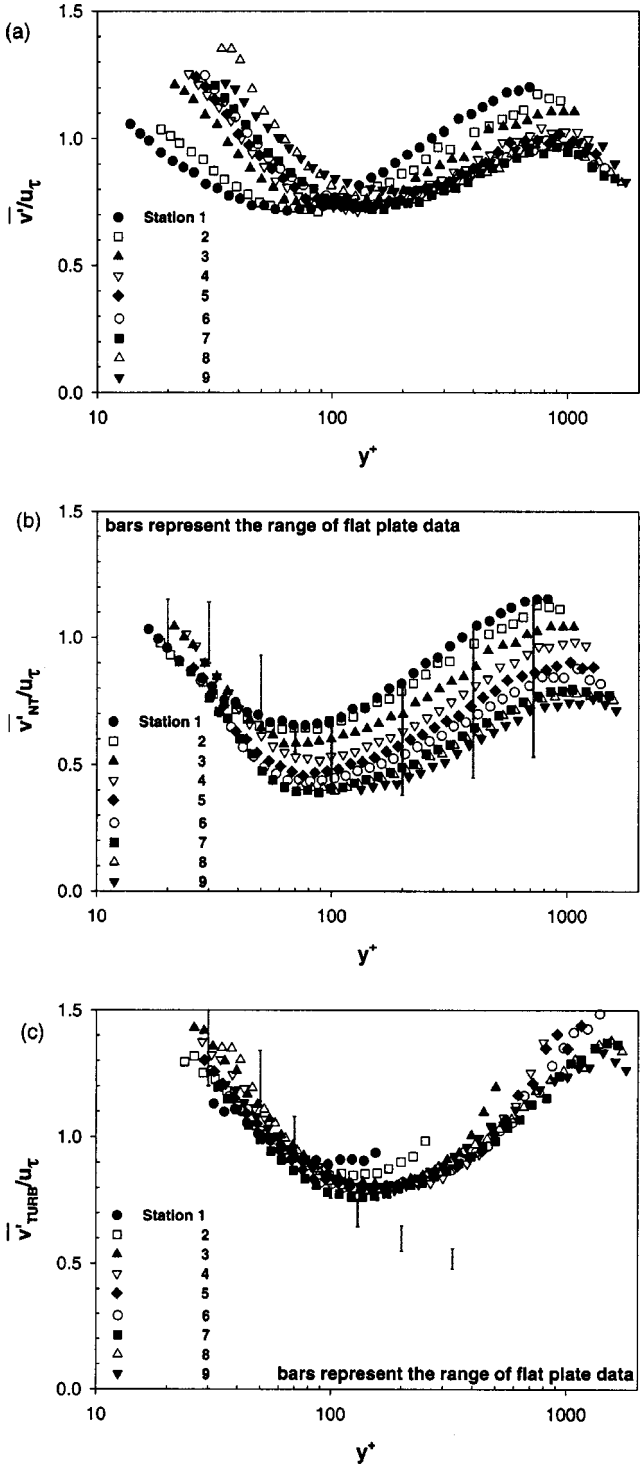

Fig. 12 Fluctuating wall-normal velocity profiles in wall coordinates: (*a*) composite; (*b*) nonturbulent; (*c*) turbulent

higher skin friction relative to near wall turbulence on the concave wall, and may be due to higher mixing in the outer part of the boundary layer. In the outer region the two data sets show good agreement in wall coordinates. Figure 11 shows the $\overline{u'}$ profiles at Station 5, midway through transition on the concave wall. The peak in $\overline{u'}$ is slightly closer to the wall in the turbulent zone, but the magnitudes of the turbulent and nonturbulent peaks are very nearly equal. The difference between the turbulent and nonturbulent zones is much reduced from the flat wall case, indicating that

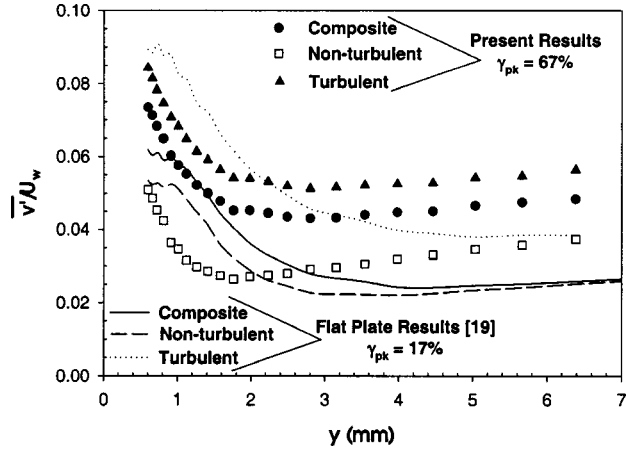

Fig. 13 Fluctuating wall-normal velocity profile for Station 5

something in the concave wall case is promoting fluctuations in the streamwise direction independent of turbulence.

Figure 12 shows the $\overline{v'}$ profiles. Figure 12(a) presents the composite flow results for the strong curvature case. The profiles are typical for a high FSTI boundary layer. They show a peak $\overline{v'}$ in the near wall region with a minimum farther from the wall followed by a rise to the freestream value. The minimum in $\overline{v'}$ results as the freestream turbulence is damped by the wall. The magnitude of $\overline{v'}/u_\tau$ rises in the near wall region as transition proceeds. As was also observed in the flat wall case of Volino et al. [19], $\overline{v'}$ is lower in magnitude and shows more change through the transition region than does $\overline{u'}$. As was the case for $\overline{u'}/u_\tau$, the turbulent zone results (Fig. 12(c)) for $\overline{v'}/u_\tau$ collapse for all of the stations. The major difference between the present results and the flat plate results is the high value of $\overline{v'}/u_\tau$ in the turbulent zone in the outer part of the boundary layer and the freestream on the concave wall. Another difference is the reduction in near wall $\overline{v'}/u_\tau$ in both zones relative to the flat wall case. As was observed for the turbulent zone $\overline{u'}/u_\tau$ profiles, higher mixing in the outer part of the concave wall boundary layer results in higher mean velocity gradients at the wall, raising the wall shear stress and u_τ. Higher u_τ reduces both $\overline{v'}/u_\tau$ and $\overline{u'}/u_\tau$ near the wall.

Figure 13 shows the $\overline{v'}$ profiles at Station 5. The magnitude of $\overline{v'}$ in the turbulent zone is almost double that in the nonturbulent zone across the entire profile. This is in contrast to the $\overline{u'}$ profiles of Fig. 11 that show the two zones to have very similar magnitudes. The same difference is also seen in the flat wall case. Volino [28] found that much of the unsteadiness in u is low-frequency unsteadiness induced by the freestream, and is a feature of both the turbulent and nonturbulent zones. The $\overline{v'}$ fluctuations, in contrast, are more closely related to near wall produced turbulence and eddy transport in the boundary layer. The differences between the turbulent and nonturbulent zones explain the rise in near wall $\overline{v'}$ in Fig. 12(a) as transition proceeds. Figure 13 also shows differences in $\overline{v'}$ between the concave and flat wall results. The concave wall $\overline{v'}$ profiles for both zones rise more rapidly near the wall, reach a minimum closer to the wall, and are higher at the edge of the boundary layer.

Turbulent Shear Stress. Turbulent shear stress profiles are shown in Fig. 14 in wall coordinates. In the composite profiles (Fig. 14(a)), the normalized turbulent shear stress increases through transition. In the nonturbulent zone the turbulent shear stress is low and comparable to the flat wall case results. In the turbulent zone (Fig. 14(c)), there is a significant increase in the normalized shear stress in the outer part of the boundary layer compared to the flat wall case. These outer region values increase

Downloaded 23 Jul 2008 to 131.122.82.145. Redistribution subject to ASME license or copyright; see http://www.asme.org/terms/Terms_Use.cfm

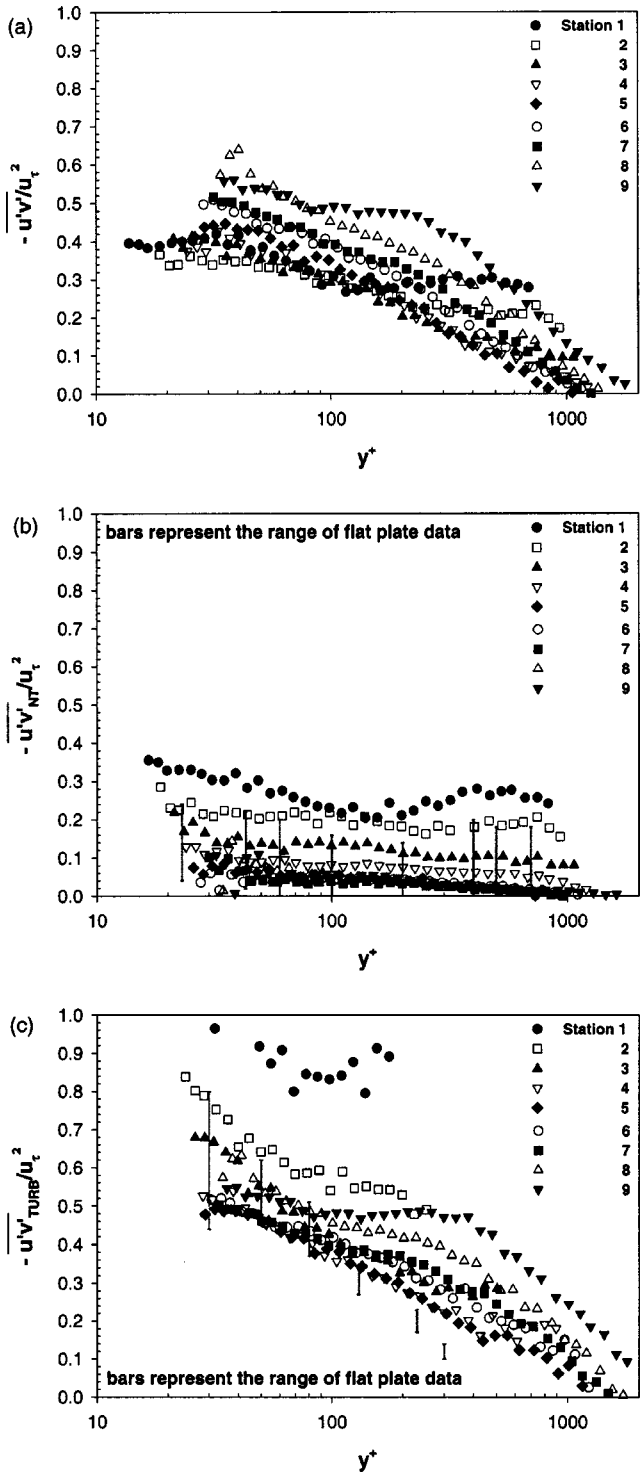

Fig. 14 Reynolds shear stress profiles in wall coordinates: (*a*) composite; (*b*) nonturbulent; (*c*) turbulent

as the flow moves downstream, presumably due to the increasing strength of curvature as the boundary layer thickens. Figure 15 presents the turbulent and nonturbulent $-\overline{u'v'}$ profiles for Station 5. Similar to $\overline{v'}$ and in contrast to $\overline{u'}$, the magnitude of $-\overline{u'v'}$ is much higher in the turbulent zone than the nonturbulent. Although $-\overline{u'v'}$ is much smaller in the nonturbulent zone, it is nonzero. This indicates that some eddy transport of momentum occurs even when the boundary layer is nonturbulent. The figure also shows that turbulent zone $-\overline{u'v'}$ is about 20% higher on the concave

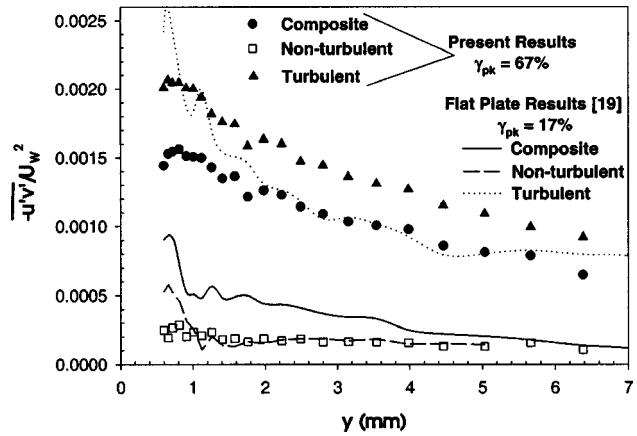

Fig. 15 Reynolds shear stress profile for Station 5

wall than on the flat wall. The composite flow $-\overline{u'v'}$ profile is higher on the concave wall due to it being further through transition than the flat wall profile at the same streamwise location.

Profiles of the eddy viscosity are presented in Fig. 16. The composite profiles in Fig. 16(a) show that ε_M increases in the streamwise direction as the transition proceeds. Comparison of the nonturbulent and turbulent zone profiles in Figs. 16(b) and 16(c) shows that the eddy viscosity is much higher in the turbulent zone. While the difference between the two zones is clear, Fig. 16(b) shows that there is still significant eddy transport in the nonturbulent zone. It is also of note that the eddy diffusivity is significantly increased on the concave wall compared to the flat wall in both the turbulent and nonturbulent zones. As was noted for the turbulent shear stress of Fig. 14(c), the turbulent zone ε_M of Fig. 16(c) increases at the downstream stations, due to the rising strength of curvature as the boundary layer grows.

Streamwise Vortices. A possible explanation for the differences between the concave and flat wall cases might be the presence of Görtler vortices in the concave wall cases. The Görtler number at Station 3 of the strong curvature case is 6, indicating that it is possible that vortices could form. No evidence of stationary Görtler vortices was observed, however. Stationary vortices would result in spanwise variation in velocity profiles, but velocity profiles measured at different spanwise location and the same streamwise location were indistinguishable. Attempts at flow visualization using smoke did not reveal Görtler vortices, although the high FSTI tended to scatter the smoke quickly, making the flow visualization results inconclusive. If vortices were present it is unlikely that they would remain stationary. In a low FSTI case vortex location would be fixed by some small upstream disturbance such as an upstream screen in a wind tunnel. In the present case, the turbulence generating grid produces large, unsteady fluctuations which might be expected to induce nonstationary vortices. Nonstationary vortices might result in high $\overline{v'}$ away from the wall as the upwash and downwash locations of the vortices moved in the spanwise direction. Spectral analysis of $\overline{v'}$ in the present case showed a broadband peak centered at 30 Hz, which was not present in the flat wall case. This along with the high $\overline{v'}$ in the outer region (Fig. 12) suggests that nonstationary vortices may be present.

Conclusions

The effect of concave curvature on transitional boundary layers subject to high freestream turbulence and strong favorable pressure gradients has been documented. Despite the strong effects of the freestream turbulence and acceleration on transition, curvature still has a significant effect. Curvature causes higher momentum transport in the outer part of the boundary layer, resulting in a

Downloaded 23 Jul 2008 to 131.122.82.145. Redistribution subject to ASME license or copyright; see http://www.asme.org/terms/Terms_Use.cfm

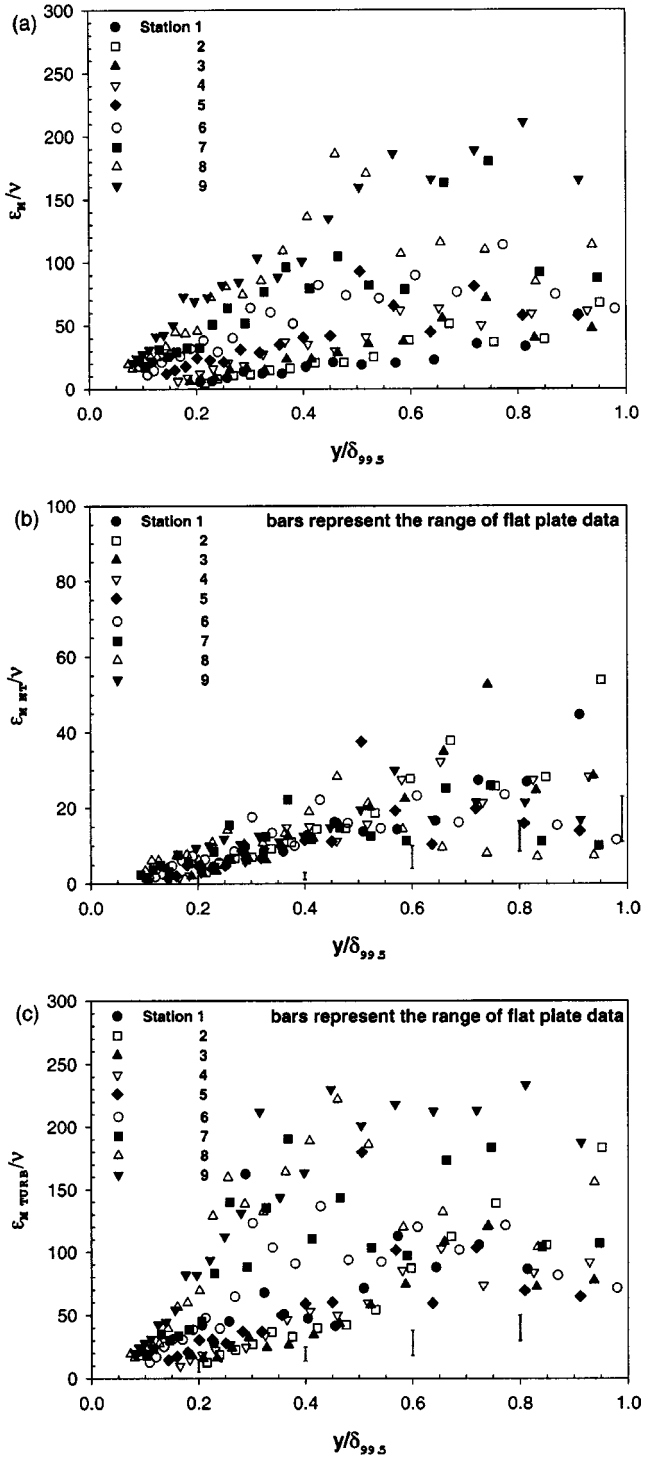

Fig. 16 Eddy viscosity profiles: (*a*) composite; (*b*) nonturbulent; (*c*) turbulent

more rapid transition to turbulence and higher skin friction. Conditional sampling shows that the curvature effect is present in both the turbulent and non-turbulent zones of the transitional flow. In the nonturbulent zone concave curvature produces mean and fluctuating velocity profiles that appear less laminar-like than in an equivalent flat wall case. In the turbulent zone curvature produces higher fluctuating velocity and turbulent shear stress in the outer part of the boundary layer. Nonstationary Görtler vortices are offered as a possible mechanism for the curvature effect on the boundary layer. Although some results which suggests the presence of vortices are presented, no direct evidence of their existence was found. Further study is needed to confirm the mechanism for the concave curvature effect.

Acknowledgments

Bill Beaver of the Technical Support Department at the U.S. Naval Academy constructed the test section. One of the authors (MPS) was supported by the Office of Naval Research as a postdoctoral fellow during the period of this work.

Nomenclature

C_f = $\tau_w/(\rho U_w^2/2)$, skin friction coefficient
FSTI = freestream turbulence intensity
$f(\gamma_{pk})$ = function of intermittency, Eq. (1)
G = $Re_\theta(\theta/r)^{0.5}$, Görtler number
H = δ^*/θ, shape factor
K = $(\nu/U_w^2)(dU_w/dx)$, acceleration parameter
$\hat{n}$ = dimensionless turbulent spot production rate
Re_x = $U_w x/\nu$, Reynolds number
Re_θ = momentum thickness Reynolds number
r = radius of curvature of test wall
U = time-averaged local streamwise velocity
U_w = local freestream velocity extrapolated to the wall
$\overline{U}_\infty$ = average freestream velocity in transition region
u = instantaneous streamwise velocity
U^+ = U/u_τ, local mean streamwise velocity in wall coordinates
$\overline{u'}$ = rms streamwise fluctuating velocity, $\sqrt{\overline{u'^2}}$
u_τ = $\sqrt{\tau_w/\rho}$, friction velocity
$-u'v'$ = instantaneous turbulent shear stress
$-\overline{u'v'}$ = time-averaged turbulent shear stress
$\overline{v'}$ = rms cross-stream fluctuating velocity, $\sqrt{\overline{v'^2}}$
x = streamwise coordinate, distance from leading edge
y = cross-stream coordinate, distance from wall
y^+ = yu_τ/ν, distance from wall-in-wall coordinates
$\delta_{99.5}$ = 99.5% boundary layer thickness
δ^* = displacement thickness
ε_M = $-\overline{u'v'}/(dU/dy)$, eddy viscosity
γ = time-averaged intermittency, fraction of time flow is turbulent
γ_{pk} = peak intermittency in profile
ν = kinematic viscosity
ρ = density
θ = momentum thickness
σ = turbulent spot propagation parameter
τ_w = wall shear stress

Subscripts

s = transition start
e = transition end
∞ = local freestream condition
w = extrapolated to the wall
NT = nonturbulent zone
TURB = turbulent zone

References

[1] Mayle, R. E., 1991, "The Role of Laminar-Turbulent Transition in Gas Turbine Engines," ASME J. Turbomach., **113**, pp. 509–537.
[2] Görtler, H., 1941, "Instabilität Laminarer Grenzchichten an Konkaven Wänder Gegenüber Gewissen Dreidimensionalen Strörungen," Z. Angew. Math. Mech., **21**, pp. 250–252 (see also NACA TM 1375, 1954).
[3] Liepmann, H. W., 1943, "Investigations on Laminar Boundary Layer Stability and Transition on Curved Boundaries," NACA Wartime Report W-87.
[4] Floryan, J. M., 1991, "On the Görtler Instability of Boundary Layers," Prog. Aerosp. Sci., **28**, pp. 235–271.
[5] Saric, W. S., 1994, "Görtler Vortices," Annu. Rev. Fluid Mech., **26**, pp. 379–409.
[6] Volino, R. J., and Simon, T. W., 1997, "Measurements in a Transitional Boundary with Görtler Vortices," ASME J. Fluids Eng., **119**, pp. 562–568.

Downloaded 23 Jul 2008 to 131.122.82.145. Redistribution subject to ASME license or copyright; see http://www.asme.org/terms/Terms_Use.cfm

[7] Finnis, M. V., and Brown, A., 1994, ''The Streamwise Development of Görtler Vortices in Favorable Pressure Gradient,'' ASME J. Turbomach., **118**, pp. 162–171.
[8] Simonich, J. C., and Moffat, R. J., 1982, ''Local Measurements of Turbulent Boundary Layer Heat Transfer on a Concave Surface Using Liquid Crystals,'' HMT-35, Thermosciences Division, Department of Mechanical Engineering, Stanford University.
[9] Kim, J., Simon, T. W., and Russ, S. G., 1992, ''Free-Stream Turbulence and Concave Curvature Effects on Heated, Transitional Boundary Layers,'' ASME J. Heat Transfer, **114**, pp. 338–347.
[10] Kestoras, M., and Simon, T. W., 1995, ''Effects of Free-Stream Turbulence Intensity on a Boundary Layer Recovering From Concave Curvature Effects,'' ASME J. Turbomach., **117**, pp. 240–247.
[11] Blair, M. F., 1983, ''Influence of Free-Stream Turbulence on Turbulent Boundary Layer Heat Transfer and Mean Profile Development: Part 1—Experimental Data,'' ASME J. Heat Transfer, **105**, pp. 33–40.
[12] Sohn, K. H., and Reshotko, E., 1991, ''Experimental Study of Boundary Layer Transition with Elevated Freestream Turbulence on a Heated Flat Plate,'' NASA CR 187068.
[13] Riley, S., Johnson, M. W., and Gibbings, J. C., 1989, ''Boundary Layer Transition of Strongly Concave Surfaces,'' ASME Paper No. 90-GT-321.
[14] Halstead, D. E., Wisler, D. C., Okiishi, T. H., Walker, G. J., Hodson, H. P., and Shin, H.-W., 1997, ''Boundary Layer Development in Axial Compressors and Turbines: Part 3 of 4—LP Turbines,'' ASME J. Turbomach., **119**, pp. 225–237.
[15] Volino, R. J., and Simon, T. W., 1997, ''Boundary Layer Transition Under High Free-Stream Turbulence and Strong Acceleration Conditions: Part 1—Mean Flow Results; Part 2— Turbulent Transport Results,'' ASME J. Heat Transfer, **119**, pp. 420–432.
[16] Volino, R. J., and Simon, T. W., 2000, ''Spectral Measurements in Transitional Boundary Layers on a Concave Wall Under High and Low Free-Stream Turbulence,'' ASME J. Turbomach., **122**, pp. 450–457.
[17] Volino, R. J., and Simon, T. W., 1995, ''Measurements in Transitional Boundary Layers under High Free-Stream Turbulence and Strong Acceleration Conditions,'' NASA CR 198413.
[18] Volino, R. J., 1998, ''A New Model for Free-Stream Turbulence Effects on Boundary Layers,'' ASME J. Turbomach., **120**, pp. 613–620.
[19] Volino, R. J., Schultz, M. P., and Pratt, C. M., 2003, ''Conditional Sampling in a Transitional Boundary Layer Under High Free-Stream Turbulence Conditions,'' ASME J. Fluids Eng., **125**, pp. 28–37.
[20] Eckert, E. R. G., 1987, ''Cross Transport of Energy in Fluid Streams,'' Waerme- Stoffuebertrag., **21**, pp. 73–81.
[21] Kestoras, M., and Simon, T. W., 1993, ''Combined Effects of Concave Curvature and High Free-Stream Turbulence Intensity on Boundary Layer Heat and Momentum Transport,'' ASME Paper No. 93-WA/HT-56.
[22] Wills, J. A. B., 1962, ''The Correction of Hot-Wire Readings for Proximity to a Solid Boundary,'' J. Fluid Mech., **12**, pp. 388–396.
[23] Volino, R. J., and Simon, T. W., 1997, ''Velocity and Temperature Profiles in Turbulent Boundary Layer Flows Experiencing Streamwise Pressure Gradients,'' ASME J. Heat Transfer, **119**, pp. 433–439.
[24] Jones, W. P., and Launder, B. E., 1972, ''Some Properties of Sink-Flow Turbulent Boundary Layers,'' J. Fluid Mech., **56**, pp. 337–351.
[25] Narasimha, R., 1985, ''The Laminar-Turbulent Transition Zone in the Boundary Layer,'' Prog. Aerosp. Sci., **22**, pp. 29–80.
[26] Volino, R. J., and Simon, T. W., 1995, ''Bypass Transition in Boundary Layers Including Curvature and Favorable Pressure Gradient Effects,'' ASME J. Turbomach., **117**, pp. 166–174.
[27] Dhawan, S., and Narasimha, R., 1958, ''Some Properties of Boundary Layer Flow During the Transition from Laminar to Turbulent Motion,'' J. Fluid Mech., **3**, pp. 418–436.
[28] Volino, R. J., 1998, ''Wavelet Analysis of Transitional Flow Data Under High Free-Stream Turbulence Conditions,'' ASME Paper No. 98-GT-289.

Downloaded 23 Jul 2008 to 131.122.82.145. Redistribution subject to ASME license or copyright; see http://www.asme.org/terms/Terms_Use.cfm